From real soils to 3D-printed soils : reproduction of complex pore network at the real size in a silty-loam soil

Nicola Dal Ferro, F Morari

SSSAJ

From real soils to 3D-printed soils: reproduction of complex pore network at the real size in a silty-loam soil

SCHOLARONE™
Manuscripts

1   **From real soils to 3D-printed soils: reproduction of complex pore network at the real size in a**

2   **silty-loam soil**

3

4   N. Dal Ferro[a], F. Morari[a*]

5   [a]*Department of Agronomy, Food, Natural resources, Animals and Environment, Agripolis,*

6   *University of Padova, Viale Dell'Università 16, 35020 Legnaro (Padova), Italy*

7

8   **Abstract**

9   Pore complexity and micro-heterogeneity are pivotal in characterizing biogeochemical processes in

10   soils. Recent advances in X-ray computed microtomography (microCT) allow the 3D soil

11   morphology characterization of undisturbed samples, although its geometrical reproduction at very

12   small spatial scales is still challenging. Here, by combining X-ray microCT with 3D multijet

13   printing technology, we aimed to evaluate the reproducibility of 3D-printing soil structures at the

14   original scale with a resolution of 80 μm and compare the hydraulic properties of original soil

15   samples with those obtained from the soil-like prototypes. Results showed that soil-like prototypes

16   were similar to the original samples in terms of total porosity and pore shape. By contrast the pore

17   connectivity was reduced by the incomplete wax removal from pore cavities after the 3D printing

18   procedure. Encouraging results were also obtained in terms of hydraulic conductivity since

19   measurements were successfully conducted on five out of six samples, showing positive correlation

20   with experimental data. We are confident that future developments of 3D-printing technologies and

21   of their combination with microCT will help to further the understanding of soil micro-

22   heterogeneity and its effects on soil-water dynamics.

23

1. INTRODUCTION

24

25   The processes that form porous media lead to highly heterogeneous three-dimensional structures,

26   forcing scientists to adopt models for reproducing the reality. This is the case for soil physics, which

27   has its foundations laid on the capillary bundle model (Hunt et al., 2013). Water flow is still

28   commonly conceptualized as a 2D bundle of cylindrical tubes passing through the soil only in the

29   vertical direction, trivializing the natural complexity of a soil. As a result, derived models such as

30   those of water conductivity (Burdine, 1953; Mualem, 1976) introduced empirical adjustments (e.g.

31   a tortuosity factor) to compensate for fundamental errors in the conceptual model (Hunt et al.,

32   2013). The simplification of reality in one-dimensional or two-dimensional models was supported

33   by the inability to see and understand the 3D structure and its interactions with biota due to its

34   opaque nature (Feeney et al., 2006). However, recent advanced technologies have provided a vast

35   amount of data and their assimilation in more complex models that have partly superseded the use

36   of reduction methods (Ahuja et al., 2006). The first steps for creating real-world situations in soil

37   science used 3D random network models (e.g., Rajaram et al., 1997; Peat et al., 2000) that

38   mimicked the soil complexity and dynamics in a three-dimensional space. In spite of their overall

39   improvement in the understanding of matrix flow and transport of solutes, these models had two

40   main limitations: a) computing limitations make some structural simplification unavoidable and b)

41   the soil has such structural complexity that a reliable estimate of a representative elementary

42   volume is difficult to quantify (Peat et al., 2000), as for most of the models. Lately, non-invasive

43   imaging approaches have gained attention as they provide the opportunity to examine soil-water

44   interactions from direct observations at the microscale. For example, the soil physical and chemical

45   processes were replicated using high-tech materials with a refractive index similar to water,

46   allowing the use of 3D optical microscopy in a transparent-reconstructed medium for the

47   visualization of biophysical processes. Controlled experiments of how pore channels can influence

2

48   the biological and hydraulic dynamics can be realized, although the reconstructed medium is only

49   partially reproducible because it is composed of single incoherent particles (Downie et al., 2012).

50   Impressive developments and insights into porous media research have also been provided by X-ray

51   computed microtomography (microCT) that allows microscopic visualization of the spatial

52   arrangement of complex structures (Cnudde and Boone, 2013). For the first time it became possible

53   to investigate the interior of an object in a non-destructive way and to extract qualitative and

54   quantitative information of multiphase porous materials (e.g., Tippkoetter et al., 2009; Mooney et

55   al., 2012). In this context "digital rock physics", i.e. the study of pore scale processes by the use of

56   digital imaging and modelling, has expanded enormously the understanding of single and

57   multiphase flow dynamics (Blunt et al., 2013).

58   Only recently 3D-printers have gained attention in the design of niche products, prototypes and one-

59   time creations (e.g., Rangel et al., 2013), although the technology is 30-years old. This technology

60   has been proposed in research as a tool to integrate virtual microCT information with real building

61   models. In fact, the combination of such techniques make it possible to reconstruct complex

62   microcosms with the heterogeneity discovered with microCT at a resolution of few micrometers,

63   providing the opportunity to isolate the physical and chemical aspects that govern the

64   biogeochemical and microbial processes in the soil (Otten et al., 2012; Ju et al., 2014; Bacher et al.,

65   2015; Ringeisen et al., 2015). Nowadays, with 3D printing the diversified geometry encountered in

66   a soil can be replicated at a resolution of tends of micrometers. Several materials can be used

67   including plastics, resins, ceramics and metals.

68   Despite large uncertainties persisting about soil microscale heterogeneity and its effects on the

69   macroscopic dynamics (Baveye et al., 2011), so far few have tried to combine high-resolution 3D

70   imaging and printing technology to improve knowledge in soil science. In this study we combined

71   3D printing technology with X-ray microCT in an attempt to reconstruct the 3D complexity of the

72   soil structure in a soil-derived model at the same spatial scale as the original one and test some

73   hydraulic properties.

74

75   **2. MATERIAL AND METHODS**

76   *Experimental design and soil sampling*

77   The soil samples come from a long-term experiment established in 1962 at the experimental farm of

78   the University of Padova (Italy). The soil (Table 1) is Fluvi-Calcaric Cambisol (CMcf), silty loam

79   (FAO-UNESCO, 1990). This work considered soil samples from a long-term trial that compares

80   two treatments: farmyard manure at 60 t ha^{-1} y^{-1} (hereafter labelled "M") and a no fertilization

81   control (hereafter labelled "C") on a continuous maize crop system. The same type of tillage has

82   been used for both treatments, with autumn plowing and subsequent cultivations prior to sowing the

83   main crop. The experimental layout is a randomized block with three replicates, on plots of 7.8 × 6

84   m. Further details on experimental design are extensively reported in the literature (e.g., Morari et

85   al., 2006). A total of six undisturbed soil cores (5 cm diameter, 6 cm length) were collected in

86   August 2010 (Fig. 1, step A), at the end of the maize season, from the topsoil (5 to 20 cm depth) in

87   polymethylmethacrylate (PMMA) cylinders using a manual hydraulic core sampler (Eijkelkamp,

88   The Netherlands). Cores were stored at 5 °C until analysis.

89

90   *MicroCT soil scanning and image processing*

91   The pore structure of soil cores, labelled "M$_{soil}$" and "C$_{soil}$" for farmyard manure and no

92   fertilization control, respectively (Fig. 1, step B) was sampled using X-ray computed

93   microtomography (microCT). In order to allow the scanning of the whole soil core at a fine

94   resolution, samples were analyzed at the "3S-R" facility in Grenoble (http://www.3sr-grenoble.fr//)

95   at a spatial resolution of 40 μm. Setting parameters were 100 kV, 300 μA and projections were

96   collected during a 360° sample rotation at 0.3° angular incremental step. Each projection was the

97   mean of 10 acquisitions and scan frequency was 7 images s^{-1}. Beam hardening artifacts were

98   minimized during data acquisition using a 0.5 mm Al filter. In order to avoid pixel misclassification

99   that might occur during projection measurements due to scattered radiation, nonlinearity of data

100   acquisition systems, partial volume effects etc. (Hsieh, 2009), 2D projections were resized after

101   acquisition using a mean filter by a two-pixel factor along the vertical and horizontal axis. As a

102   result, the reconstructed images had a coarser resolution than that of acquisition (i.e. 80 μm).

103   Resized projections were finally reconstructed using the dedicated software DigiCT 1.1 (Digisens,

104   France) to obtain a stack of about 750 2D slices in 32-bit depth. 32-bit images were later converted

105   into 8-bit depth.

106   The digital image processing and analysis of soil samples, conducted with the public domain image

107   processing ImageJ (Vs. 1.45, National Institute of Health, http://rsb.info.nih.gov/ij), has already

108   been reported in (Dal Ferro et al., 2013). Briefly, a cylindrical volume of interest with a diameter of

109   600 pixels and composed of 600 slices (4.8 cm height × 4.8 cm diameter) was selected in order to

110   exclude the PMMA sample holder. Slices were segmented using a global-threshold value based on

111   the histogram greyscale that was determined by the maximum entropy threshold algorithm. The

112   threshold value was selected where the inter-class entropy was maximized (Luo et al., 2010). 8-

113   connectivity, a mathematical morphology closing operator (Serra, 1982), was applied to the binary

114   images to fill misclassified pixels inside the pores as well as to maintain pore connections (Mooney

115   et al., 2006). Successively, the one interconnected pore network (infinite cluster) that contained

116   most of the porosity within each stack was extracted and analyzed with CTAn software v. 1.12.0.0

117   (Bruker micro-CT, Kontich, Belgium) as this pore space was the only one to show continuity

118   between the top and bottom of the soil cores. Although more connections between pores were likely

119   present within the soil cores, microCT imaging provided only connections larger than the resolution

120   limits, restricting our analysis to the soil macroporosity. A description of the soil morphological

121   parameters as a result of microCT scanning has already been reported in Dal Ferro et al. (2015)

122   (Table 1).

123

124   *3D mesh generation*

125   A surface mesh model for each sample (3 replicates × 2 treatments) was extracted from the one

126   interconnected pore network that was identified from the microCT stacks using the free software

127   InVesalius 3.0 (CTI, Campinas, São Paulo, Brazil) (Fig. 1, step G). The created model was then

128   exported in the geometrical stereolithography file format encoded in Standard Tessellation

129   Language (STL). The reconstructed STL model, composed of 10 to 30 million triangles depending

130   on the complexity of the pore network, was visualized with the open-source software MeshLab

131   v.1.3.2 (STI-CNR, Rome, Italy; http://meshlab.sourceforge.net/) in order to assess the continuity of

132   pore connections along the vertical axis and successively simplified to a polygonal mesh that

133   consisted of up to 10 million triangles. In order to compare the microCT imaging from the original

134   samples with the 3D-printed prototypes from the STL model, one of the three replicate microCT

135   stacks was selected for both "M" and "C". Afterwards a volume of interest, corresponding to a

136   cylinder of 300 pixels height × 300 pixels of diameter (Fig. 1, step C), was extracted by both

137   samples (2.4 cm high × 2.4 cm diameter). InVesalius 3.0 was used to obtain a polygonal mesh

138   model, from which a STL file was exported (Fig. 1, step D). MeshLab v.1.3.2 was used to simplify

139   the polygonal mesh at two levels of detail, corresponding to 500 thousand (500k) and 10 million

140   (10M) triangles respectively. Each model was 3D-printed twice (Fig. 1, step E), resulting in a total

141   of eight models (2 soil samples × 2 generated meshes × 2 replicate printings). All the closed pores,

142   i.e. the pores that had no connection to the space outside, were then digitally removed from the

143   stacks since they cannot contribute to flow properties of the model.

144

6

3D printing

Lastly, 14 polygonal meshes (6 cylinders, 4.8 cm h × 4.8 cm diameter; 8 cylindrical subsamples, 2.4 cm h × 2.4 cm diameter) were built with a commercial 3D printer. The printer (ProJet 3510 HD, 3D Systems, http://www.3dsystems.com/) was selected as it provided a fast prototype reconstruction with high resolution and available at a relatively low price (few hundred €). The 3D structure was printed with resin whose exact composition is proprietary but approximately contained an organic mixture of: ethoxylated bisphenol A diacrylate (15-35%), urethane acrylate oligomers (20-40 %), tripropyleneglycol diacrylate (1.5-3%) (Visijet Crystal, EX 200 Plastic material, Safety Data Sheet, http://www.3dsystems.com). The 3D printer has a multijet printing technology, i.e. an inkjet printing process that deposits either photocurable plastic resin or casting wax materials layer by layer, with a spatial resolution of 29 μm and a declared accuracy of 25-50 μm, depending on building parameters and prototype size and geometry. The final result was a set of solid prototypes whose pores were filled with paraffin wax (the contact angle between water and wax, measured with a goniometer, was 120°), while the soil matrix was composed of the resin. The contact angle between the pure resin (cleaned of any wax) and the water, measured with a contact angle goniometer, was 69°.

Wax removal procedure

Wax removal is crucial in order to empty the pores and accurately replicate the complex geometry of the soil samples. Ultrasonication in oil at a temperature of 60 °C and 60 Hz for 24 h and oven drying at 60 °C until stabilized weight (*ca.* four days) were adopted as possible procedures to empty the pores. Alternative methods were considered: the use of xylene or vapor steam cleaning would have dissolved the wax, although it would have probably corrupted the solid pore surface, while alternative printing technologies without the use of wax as a physical support during 3d printing

169   were not feasible. As a result, we adopted a simple and relatively low-cost combination between 3D

170   printing technology and cleaning procedure.

171

172   *3D prototypes scanning, image reconstruction and analysis*

173   The resulting prototypes from the sub-volume of the samples (i.e. "M_{small}" and "C_{small}" at a detail of

174   500 thousand and 10 million triangles) were finally subjected to X-ray microCT scanning (Fig. 1,

175   step F) in order to assess: a) the reproducibility and reliability of the 3D printing process; b) the

176   smoothing effect of polygon reduction on the generated 3D structure; c) efficacy of the cleaning

177   procedure to remove the wax from the pores. Prototypes were analyzed with a Skyscan 1172 X-ray

178   microtomography (Bruker micro-CT, Kontich, Belgium) at the University of Padova since lower

179   energy than those used for scanning the whole soil sample was required to penetrate the specimen.

180   Setting parameters were 40 kV, 250 µA and projections were collected during a 180° sample

181   rotation at 0.25° angular incremental step. Each projection was the mean of eight acquisitions and

182   scan frequency was 1.33 images s^{-1}. Beam hardening artifacts were minimized during data

183   acquisition using a 0.5 mm Al filter. The spatial resolution was 27 µm. In order to avoid pixel

184   misclassification that might occur during image acquisition (Hsieh, 2009), projections were resized

185   after acquisition using a mean filter by a two-pixel factor along the vertical and horizontal axis. As a

186   result, the reconstructed images had a final resolution twice that of acquisition (i.e. 54 µm). Resized

187   projections were reconstructed using the dedicated software NRecon v. 1.6.9.4 provided by Bruker

188   micro-CT to obtain a stack of about 450 2D slices in 16-bit depth. 16-bit images were later

189   converted into 8-bit depth.

190   Prototype matrix, wax and void phases were easily visualized and binarized with a single threshold

191   level. 8-connectivity was applied to the binary images to fill misclassified pixels inside the pores as

192   well as to maintain pore connections (Mooney et al., 2006). MicroCT porosity (m^3 m^{-3}), pore size

193   distribution and open porosity (%), pore surface to volume ratio (μm^{-1}), 3D fractal dimension and

194   Euler number (mm^{-3}) were estimated from each binarized stack using CTAn and compared with soil

195   parameters obtained from the original sub-volume samples.

196

197   *Hydraulic conductivity test on 3D-printed prototypes*

198   Saturated hydraulic conductivity ($K_{s\text{-}large}$) measurements were conducted on the large prototypes

199   ("M_{large}" and "C_{large}", 4.8 cm high $\times$ 4.8 cm diameter) (Fig. 1, step H) by using a laboratory

200   permeameter (Eijkelkamp, The Netherlands) that was adjusted to the size of the samples by using a

201   gasket whose thickness created a seal at the interface between the prototype and the sample holder.

202    $K_{s\text{-}large}$ was determined with both constant and variable head method, according to the hydraulic

203   properties of the medium. As a rule of thumb, $K_{s\text{-}large}$ values greater than 5.8 10^{-6} m s^{-1} were easily

204   determined by the constant head method, while the falling head method was conducted at smaller

205    $K_{s\text{-}large}$ values. Before conducting the analysis and to ensure that water flowed only vertically from

206   the top to the bottom of the prototypes, avoiding the loss of water from lateral pores, samples were

207   firstly sealed with a plastic tape and successively coated with a layer of melted wax. As a result, it

208   was ensured the complete sealing of the samples avoiding the lateral occlusion of interior pores.

209   Successively samples were freely upward saturated at atmospheric pressure (water bath reached ¾

210   of sample height) using de-aerated water, then subjected to 0.6 10^{-5} Pa to completely de-aerate them

211   and saturated again as above.

212

213   *Hydraulic conductivity test on original samples*

214   Saturated water conductivity on soil-like prototypes was compared with water flow calculated on

215   the original soil samples and already proposed in (Dal Ferro et al., 2015). As a result, original

216   samples were subjected to saturated water conductivity analyses ($K_{s\text{-}soil}$, m s^{-1}) using the constant

9

217   head or falling head method, depending on the soil properties and range of $K_{s\text{-soil}}$ that can be

218   measured (Reynolds et al., 2002). In addition, the microCT imaging dataset of the original samples

219   (scanned at the "3S-R" facility in Grenoble) was used to calculate water conductivity on the one

220   interconnected pore cluster (K_{Morph}, m s^{-1}) by using a morphologic approach as proposed by (Elliot

221   et al., 2010). Briefly, the model consisted of combining three dimensional pore shape parameters

222   with pore volume and using a modified Poiseuille equation as follows:

223    $$Q = \frac{\pi R^4 \Delta P}{8 L_c \nu} \; ,$$ [1]

224   where R is pore radius, ν is the viscosity of water at room temperature, ΔP is the change in

225   hydrostatic pressure and L_c is the pore length, depending on pore shape characteristics.

226   Lastly, rearrangement of Darcy's law allowed the K_{Morph} estimation for the extracted pore network:

227    $$K = \frac{QL}{A \Delta P} \, ,$$ [2]

228   where A is the cross-sectional area of the sample and L is the sample length. A detailed description

229   of the methods and results for the soils proposed here can be found in Dal Ferro et al. (2015).

230

231   **3. RESULTS**

232   *Soil volume and prototype measurements*

233   Ultrasonication in oil was only partially able to remove the wax from pores, while the subsequent

234   oven drying at 60 °C was able to remove most of it (Fig. 2). A further increase in temperature was

235   not possible because, according to the manufacturer, it would have weakened the resin structure or

236   melted part of it. As a result, the combination of both techniques was used as the best procedure

237   currently available to successfully empty the open pores as well as maintain the solid structure.

238   However, the continuing advances in 3D-printing technology and the use of heat-resistant materials

239   will allow the full removal of the support material (e.g. by evaporation).

240   Soil porosity of sub-volumes scanned with microCT   ("M_{soil}" and "C_{soil}" 2.4 cm high × 2.4 cm

241   diameter) was entirely connected to the space outside the soil matrix (open pores/total porosity =

242   100%), but highly different between "M_{soil}" (0.114) and "C_{soil}" (0.036) (Table 2). The open pores of

243   "M_{small}" prototypes were slightly lower than porosity detected by microCT, with negligible changes

244   between 500 thousand (500k) and 10 million (10M) triangle meshes. Indeed, only 2.4% of microCT

245   porosity (0.109 and 0.110 in 500k and 10M, respectively) was confined within the solid phase

246   (Table 2). By contrast, the "C_{small}" prototypes showed a consistent increase of confined pores with

247   respect to the total ones, ranging from 15.1% in the 500k to 18.4% in the 10M meshes, on average.

248   As a result, the "C_{soil}" porosity (0.036) was slightly greater than "C_{small}" built both from 500

249   thousand (0.024) and 10 million (0.027) triangle meshes respectively.

250   Pore size distribution (PSD) curves (Fig. 4), measured on microCT images in volumetric terms

251   according to the medial-axes determination and sphere-fitting measurement (Remy and Thiel,

252   2002), were distributed differently between "M" and "C". In "M" the most frequent pore classes

253   were distributed between 240 μm and 560 μm diameter, while they were shifted towards smaller

254   pores in "C", ranging between 160 μm and 440 μm. Comparable data were found between PSD

255   prototype classes, in both "M" and "C", with negligible variations between replicates and meshes.

256   By contrast, a sharp increase of the small pores was observed in the original samples with respect to

257   the prototypes: this was particularly clear for pore classes smaller than 800 μm and 490 μm in

258   "M_{soil}" and "C_{soil}", where the integral of the PSD differences was around 30% and 10% of microCT

259   porosity, respectively. Finally, it was noticed that some pores were still filled with wax despite its

260   melting and removal with ultrasonication and oven drying (Fig. 3). In particular, wax most resided

261   in thin throats (< 200 μm, on average) between largest cavities, leading to their disconnection and

262   thus increasing both the average size of empty pores and the number of isolated ones.

263   Pore morphological features (Table 2), estimated by means of pore surface/volume ratio (μm^{-1}),

264   Euler number (i.e. an indicator of pore connectivity, where the greater is the value, the lower is the

265   pore connectivity; mm^{-3}) (Vogel et al., 2010) and 3D fractal dimension (box-counting method)

266   (Perret et al., 2003), emphasized the self-similarity between the prototypes that were generated by

267   the same original sub-volume. For instance, the pore surface/volume ratio was 0.007 μm^{-1} in

268   "M_{small}" prototypes as characterized by different meshes (500k and 10M triangles), while the fractal

269   dimension (2.42 and 2.25 in the original "M_{soil}" and "C_{soil}", respectively) ranged in "M_{small}"

270   between 2.10 (500k triangles) and 2.62 (10M triangles) and in "C_{small}" between 2.38 (500k

271   triangles) and 2.55 (10M triangles). Only the Euler number parameter, particularly in "M_{small}" and

272   "C_{small}" built from 500k triangle meshes, showed high variability between the prototypes (Table 2).

273

274   *Experimental saturated hydraulic conductivity measurements on large prototypes*

275   Experimental saturated hydraulic conductivity ($K_{s\text{-large}}$) data were obtained on five of the six

276   reconstructed large prototypes ("M_{large}" and "C_{large}" 4.8 cm high $\times$ 4.8 cm diameter, an example is

277   reported in Fig. 5) since water did not flow through one of the "C_{large}" samples (Table 3). $K_{s\text{-large}}$

278   was generally higher in "M" (18.5 m s^{-1}, on average) than "C" (0.035 m s^{-1}, on average), ranging

279   between a minimum of 0.023 m s^{-1} observed in "C" and a maximum of 13.5 m s^{-1} in "M. The water

280   flow measurements on the prototypes were generally greater (7.65 10^{-5} m s^{-1}, on average) than those

281   measured ($K_{s\text{-soil}}$ = 3.59 10^{-6}, on average) and modelled (K_{Morph} = 1.91 10^{-6} m s^{-1}) on the original soil

282   samples (Table 3) (Dal Ferro et al., 2015). Finally, positive correlations were observed between

283   soil-like $K_{s\text{-large}}$ values and both $K_{s\text{-soil}}$ (R^2 = 0.69) and K_{Morph} (R^2 = 0.93, Fig. 6).

284

285   **4. DISCUSSION**

286   The comparison between morphological characteristics of replicated small prototypes ("M_{small}" and

287   "C_{small}") showed that 3D printing technology was able to retain the basic features of the macropore

288   network. More specifically, the pore size and shape characteristics of the largest pores was easily

289   visualized on the microCT imaging (Fig. 3), highlighting the similarity between reconstructed

290   models. Moreover, introducing some smoothing of the surface walls by the simplification of the

291   mesh (500 thousand *vs*. 10 million triangles) did not show significant changes between macropore

292   characteristics. In particular, the "M" microCT porosity and pore surface/volume ratio had a

293   coefficient of variation of 3.6% and 4.8%, respectively. These results were supported by others:

294   Otten et al. (2012) reported a very high reproducibility of twelve prototypes since the measured

295   porosity (0.66) was characterized by a very low coefficient of variation (3.36%), although their soil-

296   like prototypes were scaled up three times with respect to the original size of the soil samples. By

297   contrast, our prototypes were reconstructed at the real size, although the soil microscale

298   heterogeneity that was provided by the fine silt and clay particles could not be faithfully reproduced

299   due to the microCT soil scanning (40 μm) and 3D printing resolution limits (29 μm).

300   The successful reproduction of generated "M_{small}" prototypes (Fig. 1, step E) was partly reappraised

301   by evaluating the pore morphological characteristics in detail (Table 2). In fact, the pore structure

302   parameters varied between the reconstructed models, especially in the "C_{small}" prototypes. For

303   instance, the coefficient of variation of total porosity was 11.5% in the "C_{small}" prototypes,

304   increasing to 63% in the Euler number. Nevertheless, it is worth noticing that the microCT scanning

305   of small prototypes (Fig. 1, step F) was performed at a resolution (27 μm) that was finer than that

306   used during the 3D-printing (29 μm, ± 50 μm), emphasizing the systematic errors during the model

307   building process. As a result, the mismatch observed between soil samples ("M_{soil}" and "C_{soil}") and

308   prototypes ("M_{small}" and "C_{small}") structures were the result of the combined effect between: a) soil

309   digital imaging due to microCT scanning; b) inaccuracy during the 3D printing process; c)

310   prototype digital imaging due to microCT scanning. Furthermore, the 3D mesh generation created

311   distorted elements from the voxel-based microCT volumes, although the negligible variations

312   between small prototypes as printed from 500 thousand and 10 million triangles suggested their

313   minor role during the prototypes production. Moreover, the partial effectiveness of wax removal

314   from the macropores (Fig. 3), quantified at around 2.4% ("M_{small}") and 16.7% ("C_{small}") of microCT

315   porosity, increased the uncertainty on the pore quantity and morphology. Finally, the biggest

316   differences were observed in terms of Euler number, showing its ability to identify slight structure

317   changes between replicated prototypes. The wax entrapped in the voids created a discontinuity

318   between adjacent pores by modifying the degree of connection of the macropore network and partly

319   isolating them from the space outside the solid matrix. As a result, the soil volumes ("M_{soil}" and

320   "C_{soil}") generally had both a higher microCT total porosity and a lower Euler number (i.e. more

321   connections) than the reconstructed prototypes (Table 2). As suggested by the pore size distribution

322   analysis, the wax was easily removed from the largest pores, while it consistently remained in the

323   smallest ones (Fig. 4). Finally, a mismatch between soil and soil-like porosity was probably

324   introduced during microCT soil analysis and the following mesh generation. Indeed microCT

325   imaging was composed of cubic voxels while polygonal mesh comprised a surface triangulation,

326   avoiding their full overlap.

327   In spite of the difficulty in totally cleaning the wax from the macropores, measurements of saturated

328   hydraulic conductivity were successfully conducted on five of the six large prototypes. Only the

329   saturated conductivity measurement on one "C_{large}" prototype failed. Since one of the "C_{large}" soil-

330   derived model was characterized by the lowest total porosity (0.015), most likely the entrapped wax

331   occluded the scarce conductive pores within the whole prototype and prevented flow. Water flow

332   measurements, calculated through the one interconnected macropore network that spanned the

333   sample, were highly correlated with properties calculated on the original samples ($K_{s\text{-}soil}$) and

334   particularly with those modelled (K_{Morph}) on the same pore network (Fig. 6) (Dal Ferro et al., 2015).

335   Nevertheless, $K_{s\text{-}large}$ had higher values than $K_{s\text{-}soil}$ and K_{Morph} by at least one order of magnitude in

336   the "M" treatment (Table 3), although the total porosity had been reduced with respect to the soil

337   sample ones in two ways: a) the prototypes were reconstructed on the basis of digital imaging from

338   microCT scanning that performed at a resolution that excluded all the small connections between

339   the largest pores and decreased the adsorption along the macropore walls; b) part of microCT

340   porosity was probably still filled with wax during $K_{s-large}$ measurements, reducing the water flow

341   capacity of the porous medium. These results suggested the major role of conducting macropores on

342   water flow dynamics (Jarvis, 2007), although the undetected and unprinted micropores < 80 μm

343   might have partially increased $K_{s-large}$ to approach the experimental K_{s-soil} (Elliot et al., 2010),

344   particularly when the soil structure was largely composed of thin pores and microcracks are often

345   insufficiently imaged with microCT and thus underrepresented (i.e. in the control samples),

346   especially in the vicinity of grain contacts (Andrä et al., 2013). Some smoothing of the pore

347   surfaces, introduced during the prototype generation, decreased the friction factor between the

348   liquid and solid phases with respect to the original samples, as was shown by the results of pore

349   surface/volume ratio (Table 2). This would have reduced the pressure drop (Kumar et al., 2011) at

350   high $K_{s-large}$ values, obeying the dynamics on the viscous forces as described in the Stokes

351   equations, while with low water velocity the difference between $K_{s-large}$ and K_{s-soil} and K_{Morph} was

352   strongly reduced. By contrast, the contact angle between the water and the solid walls (69°) was

353   only a minor factor for influencing the water movement, although it is reasonable that, despite the

354   emptying procedure, the pores were still coated with wax that would have induced fluid slip for

355   water flowing over a hydrophobic surface (Tretheway and Meinhart, 2002).

356

357   **5. CONCLUSIONS**

358   Integrating X-ray microtomography and 3D printing technology is feasible in soil science at the

359   microscale and provides great opportunities to better understand the role of micro-heterogeneity in

360   the soil-water dynamics. In particular, soil-like prototypes were built with relatively large

15

361 replicability and similarity to the original ones at the actual size, with a resolution of 80 μm.

362 Moreover, the mesh simplification (from 100 million to 500 thousand triangles) did not reveal

363 significant differences between prototypes. By contrast, the full wax removal from the pores was

364 not completely solved as it limited the pore connectivity and increased the surface smoothing.

365 Nevertheless, water conductivity was successfully performed on five of the six large prototypes,

366 showing a strong correlation with experimental and modelled data from the original soil samples.

367 The comparison between $K_{s-large}$ (i.e. on prototypes) and K_{Morph} (morphologic model) data,

368 performed on the same porous systems, highlighted the major role of the macropore surface

369 smoothing and the hydrophobic nature of wax. In particular, an increase of fluid slip and

370 consequently of water velocity at laminar flow was observed for $K_{s-large} \geq 10^{-5}$ m s^{-1}, while it was

371 consistently reduced at lower values. By contrast, the detection of micropores < 80 μm would have

372 approached the $K_{s-large}$ values to reach the experimental ones (K_{s-soil}), especially at low water

373 velocities. In order to promote a broad application of 3D prototypes in the hydrological research,

374 future application of 3D printing technology should address many technological challenges. In fact

375 a higher microCT scanning and 3D-printed resolution will favor the representation of the soil pore

376 system at the nanoscale and its heterogeneity. Moreover the use of soil-like materials will be able to

377 model the physical-chemical interaction between water and the pore surface. Nevertheless, even at

378 this stage, our work suggests as 3D printing technology can represent a breakthrough technology for

379 the study of soil structure and its interaction with biogeochemical processes.

380

381

382 **REFERENCES**

383 Ahuja, L.R., L. Ma, and D.J. Timlin. 2006. Trans-disciplinary soil physics research critical to

384 synthesis and modeling of agricultural systems. Soil Sci. Soc. Am. J. 70:311-326.

385 doi:10.2136/sssaj2005.0207

386   Andrä, H., N. Combaret, J. Dvorkin, E. Glatt, J. Han, M. Kabel, Y. Keehm, F. Krzikalla, M. Lee,

387   and C. Madonna. 2013. Digital rock physics benchmarks-part II: Computing effective properties.

388   Comput. Geosci. 50:33-43. doi:10.1016/j.cageo.2012.09.008

389   Baveye, P.C., D. Rangel, A.R. Jacobson, M. Laba, C. Darnault, W. Otten, R. Radulovich, and

390   F.A.O. Camargo. 2011. From dust bowl to dust bowl: soils are still very much a frontier of science.

391   Soil Sci. Soc. Am. J. 75:2037-2048. doi:10.2136/sssaj2011.0145

392   Bacher, M., Schwen, A., and Koestel, J. 2015. Three-dimensional printing of macropore networks

393   of an undisturbed soil sample. Vadose Zone J. 14:1-10. doi:10.2136/vzj2014.08.0111

394   Blunt, M.J., B. Bijeljic, H. Dong, O. Gharbi, S. Iglauer, P. Mostaghimi, A. Paluszny, and C.

395   Pentland. 2013. Pore-scale imaging and modelling. Adv. Water Resour. 51:197-216. doi:

396   10.1016/j.advwatres.2012.03.003

397   Burdine, N.T. 1953. Relative permeability calculations from pore size distribution data. J. Pet.

398   Technol. 5:71-78. doi:http://dx.doi.org/10.2118/225-G

399   Cnudde, V., and M.N. Boone. 2013. High-resolution X-ray computed tomography in geosciences:

400   A   review   of   the   current   technology   and   applications.   Earth-Sci.   Rev.   123:1-17.

401   doi:10.1016/j.earscirev.2013.04.003

402   Dal Ferro, N., P. Charrier, and F. Morari. 2013. Dual-scale micro-CT assessment of soil structure in

403   a long-term fertilization experiment. Geoderma 204:84-93. doi:10.1016/j.geoderma.2013.04.012

404   Dal Ferro, N., A.G. Strozzi, C. Duwig, P. Delmas, P. Charrier, and F. Morari. 2015. Application of

405   smoothed particle hydrodynamics (SPH) and pore morphologic model to predict saturated water

406   conductivity from X-ray CT. Geoderma 255:27-34. doi:10.1016/j.geoderma.2015.04.019

407   Downie, H., N. Holden, W. Otten, A.J. Spiers, T.A. Valentine, and L.X. Dupuy. 2012. Transparent

408   soil for imaging the rhizosphere. PloS ONE. 7:e44276. doi:10.1371/journal.pone.0044276

409   Elliot, T.R., W.D. Reynolds, and R.J. Heck. 2010. Use of existing pore models and X-ray computed

410   tomography   to   predict   saturated   soil   hydraulic   conductivity.   Geoderma   156:133-142.

411   doi:10.1016/j.geoderma.2010.02.010

412   FAO-UNESCO. 1990. Soil map of the world. Revised Legend. FAO, Rome.

413   Feeney, D.S., J.W. Crawford, T. Daniell, P.D. Hallett, N. Nunan, K. Ritz, M. Rivers, and I.M.

414   Young. 2006. Three-dimensional microorganization of the soil–root–microbe system. Microb. Ecol.

415   52:151-158. doi:10.1007/s00248-006-9062-8

416   Hsieh, J. 2009. Computed tomography: Principles, design, artifacts, and recent advances. Second

417   ed. SPIE Bellingham, Washington, USA.

418   Hunt, A.G., R.P. Ewing, and R. Horton. 2013. What's wrong with soil physics? Soil Sci. Soc. Am.

419   J. 77:1877-1887. doi:10.2136/sssaj2013.01.0020

420   Jarvis, N.J. 2007. A review of non-equilibrium water flow and solute transport in soil macropores:

421   principles, controlling factors and consequences for water quality. Eur. J. Soil Sci. 58:523-546.

422   doi:10.1111/j.1365-2389.2007.00915.x

423   Ju, Y., H. Xie, Z. Zheng, J. Lu, L. Mao, F. Gao, and R. Peng. 2014. Visualization of the complex

424   structure and stress field inside rock by means of 3D printing technology. Chin. Sci. Bull. 59:5354-

425   5365. doi:10.1007/s11434-014-0579-9

426   Kumar, V., M. Paraschivoiu, and K.D.P. Nigam. 2011. Single-phase fluid flow and mixing in

427   microchannels. Chem. Eng. Sci. 66, 1329-1373. doi:10.1016/j.ces.2010.08.016

428   Luo, L., H. Lin, S. Li. 2010. Quantification of 3-D soil macropore networks in different soil types

429   and   land   uses   using   computed   tomography.   J.   Hydrol.   393:53-64.

430   doi:10.1016/j.jhydrol.2010.03.031

431   Mooney, S.J., C. Morris, and P.M. Berry. 2006. Visualization and quantification of the effects of

432   cereal root lodging on three-dimensional soil macrostructure using X-ray computed tomography.

433   Soil Sci. 171:706-718. doi:10.1097/01.ss.0000228041.03142.d3

434   Mooney, S.J., T.P. Pridmore, J. Helliwell, and M.J. Bennett. 2012. Developing X-ray Computed

435   Tomography to non-invasively image 3-D root systems architecture in soil. Plant Soil. 352:1-22.

436   doi:10.1007/s11104-011-1039-9

437   Morari, F., E. Lugato, A. Berti, and L. Giardini. 2006. Long-term effects of recommended

438   management practices on soil carbon changes and sequestration in north-eastern Italy. Soil Use

439   Manage. 22:71-81. doi:10.1111/j.1475-2743.2005.00006.x

440   Mualem, Y. 1976. A new model for predicting the hydraulic conductivity of unsaturated porous

441   media. Water Resour. Res. 12:513-522. doi:10.1029/WR012i003p00513

442   Otten, W., R. Pajor, S. Schmidt, P.C. Baveye, R. Hague, and R.E Falconer. 2012. Combining X-ray

443   CT and 3D printing technology to produce microcosms with replicable, complex pore geometries.

444   Soil Biol. Biochem. 51:53-55. doi:10.1016/j.soilbio.2012.04.008

445   Peat, D.M.W., G.P. Matthews, P.J. Worsfold, and P.J., and S.C Jarvis. 2000. Simulation of water

446   retention and hydraulic conductivity in soil using a three-dimensional network. Eur. J. Soil Sci.

447   51:65-79. doi:10.1046/j.1365-2389.2000.00294.x

448   Perret, J.S., S.O. Prasher, and A.R. Kacimov. 2003. Mass fractal dimension of soil macropores

449   using computed tomography: from the box-counting to the cube-counting algorithm. Eur. J. Soil

450   Sci. 54:569-579. doi:10.1046/j.1365-2389.2003.00546.x

451   Rajaram, H., L.A. Ferrand, and M.A. Celia. 1997. Prediction of relative permeabilities for

452   unconsolidated soils using pore-scale network models. Water Resour. Res. 33:43-52.

453   doi:10.1029/96WR02841

454   Rangel, D.P., C. Superak, M. Bielschowsky, K. Farris, R.E. Falconer, and P.C. Baveye. 2013.

455   Rapid prototyping and 3-D printing of experimental equipment in soil science research. Soil Sci.

456   Soc. Am. J. 77:54-59. doi:10.2136/sssaj2012.0196n

457   Remy, E., Thiel, E., 2002. Medial axis for chamfer distances: computing look-up tables and

458   neighbourhoods in 2D or 3D. Pattern Recogn. Lett. 23:649–661. doi:10.1016/S0167-

459   8655(01)00141-6

460   Reynolds, W.D., D.E. Elrick, E.G. Youngs, A. Amoozegar, H.W.G. Booltink, and J. Bouma. 2002.

461   3.4 Saturated and field-saturated water flow parameters. p. 797-801. In J.H. Dane and G.C. Topp

462   (ed.) Methods of Soil Analysis Part 4 - Physical Methods. SSSA Madison, WI

463   Ringeisen, B.R., K. Rincon, L.A. Fitzgerald, P.A. Fulmer, and P.K. Wu. 2015. Printing soil: a

464   single-step, high-throughput method to isolate micro-organisms and near-neighbour microbial

465   consortia from a complex environmental sample. Methods Ecol. Evol. 6:209-217.

466   doi:10.1111/2041-210X.12303

467   Serra, J. 1992. Image analysis and mathematical morphology. Academic Press, London, UK.

468   Tippkoetter, R., T. Eickhorst, H. Taubner, B. Gredner, and G. Rademaker. 2009. Detection of soil

469   water in macropores of undisturbed soil using microfocus X-ray tube computerized tomography

470   (μCT). Soil Till. Res. 105:12-20. doi:10.1016/j.still.2009.05.001

471 Tretheway, D.C., and C.D. Meinhart. 2002. Apparent fluid slip at hydrophobic microchannel walls.

472 Phys. Fluids. 14:L9-L12. doi:0.1063/1.1432696

473 Vogel, H.J., U. Weller, and S. Schlüter. 2010. Quantification of soil structure based on Minkowski

474 functions. Comput. Geosci. 36:1236-1245. doi:10.1016/j.cageo.2010.03.007

475

476   **Captions of figures**

477   **Figure 1** Outline of steps used to obtain soil-like prototypes and sample measurements.

478   **Figure 2** 2D slices from microCT imaging (M = farmyard manure; C = control) of original soil
479   samples (A1, B1) and soil-like prototypes after the wax removal procedure with ultrasonication
480   (A2, A3, B2, B3) and oven drying (A4, B4).

481   **Figure 3** 2D slices from microCT imaging of original soil samples (A1, B1) and soil-like
482   prototypes (M = farmyard manure; C = control). Prototypes were obtained in duplicate from a
483   polygonal mesh composed of both 500 thousand (500k; A2, A5, B2, B5) and 10 million (10M; A3,
484   A6, B3, B6) triangles. Grayscale images are composed of empty pores (black objects) and solid
485   material (gray objects). Binary images are composed of empty pores (white) and solid material
486   (black).

487   **Figure 4** Pore size distribution estimated by means of X-ray microCT on original soil samples
488   ("M_{soil} and "C_{soil}") and on soil-like prototypes ("M_{small}" and "C_{small}") from 3D printing at different
489   mesh accuracy (500k = 500 thousand triangles; 10M = ten million triangles).

490   **Figure 5** 3D representations of a large soil sample (farmyard manure treatment) as a result of X-ray
491   microCT analysis (A, C; spatial resolution of 40 μm) and pictures of its 3D-printed copy (B, D;
492   spatial resolution of 29 μm).

493   **Figure 6** Relationship between saturated water conductivities estimated on soil-like prototypes ($K_{s\text{-}large}$, m s^{-1}) and on the original soil samples by means of (A) experimental ($K_{s\text{-}soil}$, m s^{-1}) and (B)
495   modelling (K_{Morph}, m s^{-1}) approach.

496   **Table 1** Texture and microCT pore morphological parameters of original soil cores (4.8 cm high × 4.8 cm diameter). Standard error values are
497   reported in brackets.

		Soil physical properties				MicroCT parameters			
ID	Replicate	Sand (%)	Silt (%)	Clay (%)	Total porosity[a] (m^3 m^{-3})	MicroCT porosity (m^3 m^{-3})	Mean pore diameter[b] (μm)	Pore surface/volume ($μm^{-1}$)	Euler number (mm^{-3})
M	1	32.1	63.3	4.7	0.490	0.086	783.74	0.008	0.31
M	2	32.0	63.3	4.7	0.461	0.102	530.24	0.011	1.09
M	3	30.0	65.0	5.0	0.476	0.045	883.97	0.009	0.16
Average		31.4(0.7)	63.9(0.6)	4.8(0.1)	0.476(0.008)	0.078(0.017)	732.65(105.26)	0.009(0.001)	0.52(0.29)
C	1	27.5	65.7	6.7	0.459	0.015	386.96	0.011	0.16
C	2	37.8	57.2	5.0	0.432	0.020	338.58	0.014	0. 6
C	3	32.6	62.0	5.4	0.439	0.033	374.06	0.013	3.13
Average		32.6(3.0)	61.6(2.5)	5.7(0.5	0.443(0.008)	0.023(0.005)	366.53(14.46)	0.013(0.001)	1.65(1.21)

498   [a]Gravimetric method with water saturation.
499   [b]Weighted mean of soil pore size distribution.
500

22

Table 2 3D parameters from microCT scanning of original soil volumes ("M_{soil}" and "C_{soil}") and soil-like prototypes ("M_{small}" and "C_{small}"). Soil and soil-like volumes were 2.4 cm high × 2.4 cm diameter. Standard error values are reported in brackets.

ID	Sample scanned	Mesh[a]	MicroCT porosity (m^3 m^{-3})	Open pores/total porosity (%)	Mean pore diameter[b] (μm)	Pore surface/volume (μm^{-1})	Euler number (mm^{-3})	3D fractal dimension
M_{soil}	Soil	-	0.114	100.00	858.60	0.007	0.42	2.41
M_{small}	Prototype	500k	0.113	98.97	925.60	0.007	3.54	2.61
M_{small}	Prototype	500k	0.106	96.36	943.26	0.007	0.82	2.10
M_{small}	Prototype	10M	0.113	98.71	940.04	0.007	1.70	2.62
M_{small}	Prototype	10M	0.107	96.32	953.31	0.007	0.97	2.17
Average	Prototype	-	0.110 (0.002)	97.591(0.84)	940.55(6.62)	0.007(0.000)	1.758(0.72)	2.38(0.16)
C_{soil}	Soil	-	0.036	100.00	319.02	0.014	0.33	2.25
C_{small}	Prototype	500k	0.027	90.30	397.66	0.013	0.981	2.40
C_{small}	Prototype	500k	0.022	79.59	393.33	0.013	0.171	2.55
C_{small}	Prototype	10M	0.028	86.35	380.00	0.013	0.795	2.38
C_{small}	Prototype	10M	0.025	76.90	246.21	0.026	1.509	2.46
Average	Prototype	-	0.026(0.002)	83.28(3.54)	354.30(41.83)	0.016(0.004)	0.864(0.319)	2.45(0.04)

[a]500k = 500 thousand tringle mesh; 10M = 10 million triangle mesh.
[b]Weighted mean of soil-like prototypes pore size distribution.

23

508 **Table 3** Experimental saturated conductivity values ($K_{s-large}$, m s^{-1}) estimated on soil-like prototypes ("M$_{large}$" and "C$_{large}$", 4.8 cm high × 4.8 cm
509 diameter) and compared with experimental (K_{s-soil}) and modelled (K_{Morph}) ones on the original soil samples. Standard error values are reported in
510 brackets.

511

ID	Replicate	$K_{s-large}$ (10^{-6} m s^{-1})	K_{s-soil}[a] (10^{-6} m s^{-1})	K_{Morph}[a] (10^{-6} m s^{-1})
M	1	134.94	6.31	5.17
M	2	19.46	2.41	4.13
M	3	30.50	3.41	1.74
Average		61.63 (36.79)	4.04 (1.17)	3.68 (1.02)
C	1	N/A	5.27	0.04
C	2	0.23	2.22	0.16
C	3	0.47	1.90	0.24
Average		0.35 (0.12)	3.13 (1.07)	0.15 (0.06)

512 [a]data from Dal Ferro et al. (2015).

513

514

515

516

517
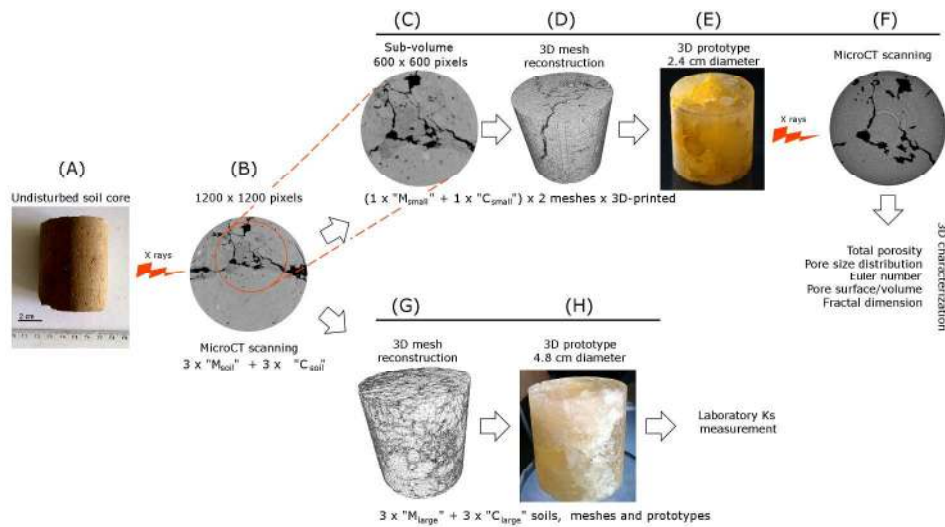
Figure 1 Outline of steps used to obtain soil-like prototypes and sample measurements.
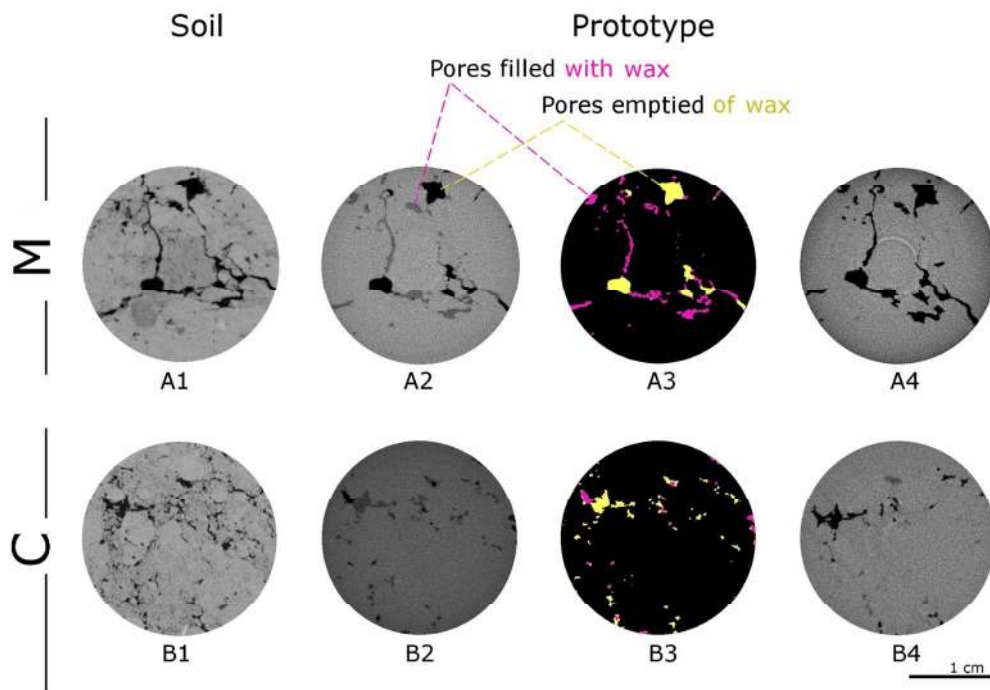216x127mm (300 x 300 DPI)

Figure 2: 2D slices from microCT imaging (M = farmyard manure; C = control) of original soil samples (A1, B1) and soil-like prototypes after the wax removal procedure with ultrasonication (A2, A3, B2, B3) and oven drying (A4, B4).
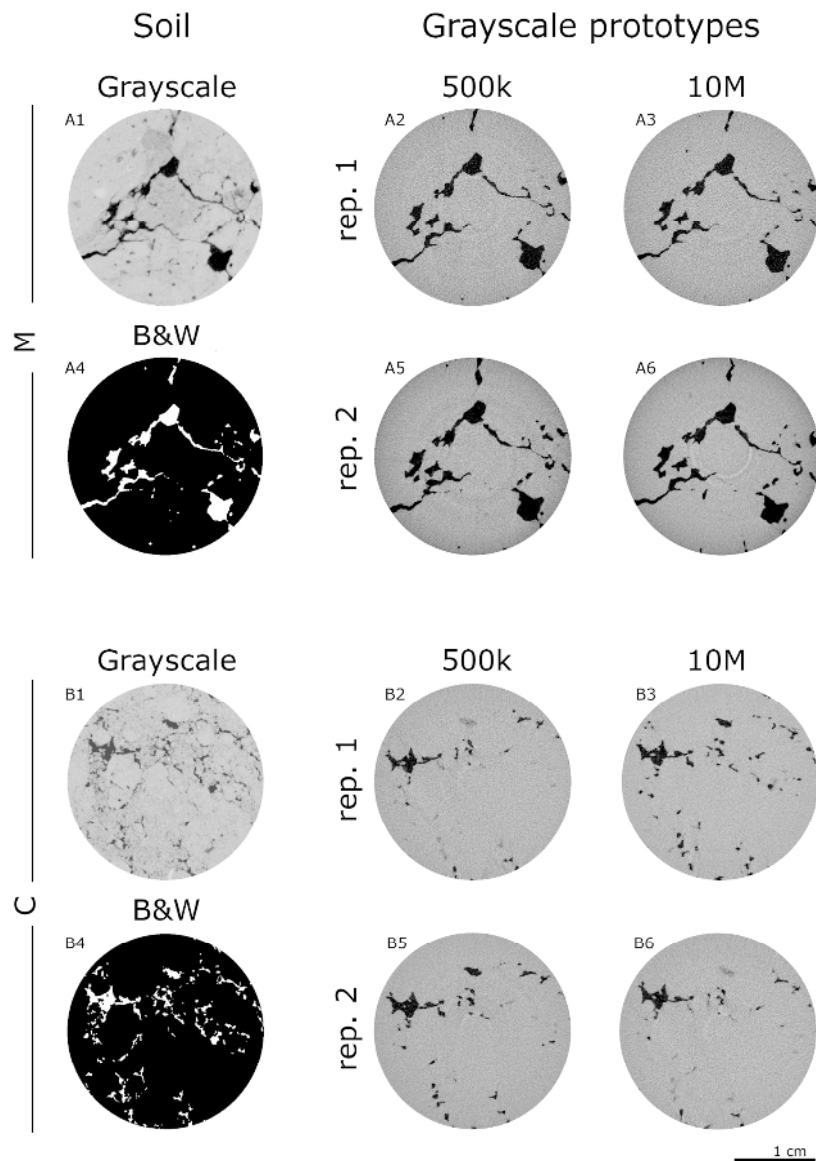152x111mm (300 x 300 DPI)

Figure 3 2D slices from microCT imaging of original soil samples (A1, B1) and soil-like prototypes (M = farmyard manure; C = control). Prototypes were obtained in duplicate from a polygonal mesh composed of both 500 thousand (500k; A2, A5, B2, B5) and 10 million (10M; A3, A6, B3, B6) triangles. Grayscale images are composed of empty pores (black objects) and solid material (gray objects). Binary images are composed of empty pores (white) and solid material (black).
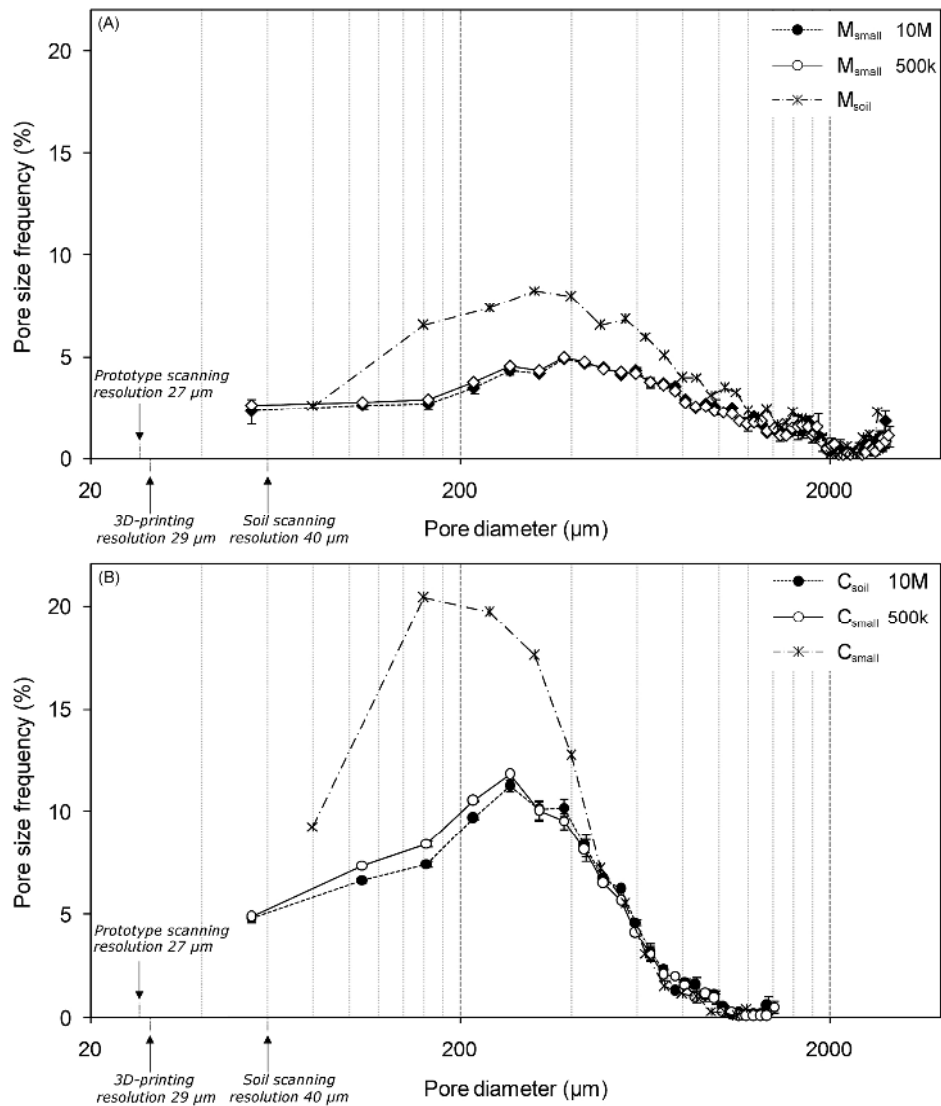119x160mm (300 x 300 DPI)

Figure 4: Pore size distribution estimated by means of X-ray microCT on original soil samples ("Msoil and "Csoil") and on soil-like prototypes ("Msmall" and "Csmall") from 3D printing at different mesh accuracy (500k = 500 thousand triangles; 10M = ten million triangles).
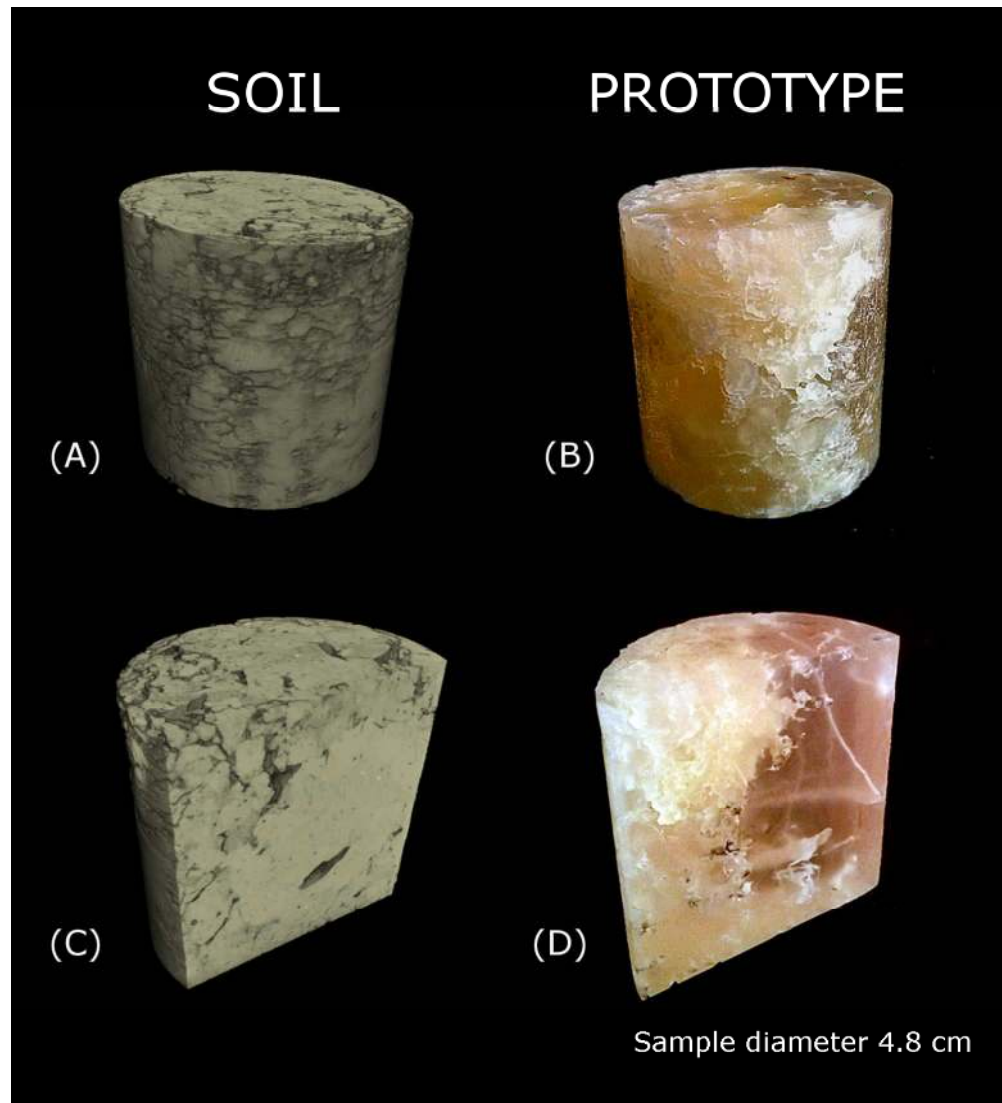169x197mm (300 x 300 DPI)

Figure 5: 3D representations of a large soil sample (farmyard manure treatment) as a result of X-ray microCT analysis (A, C; spatial resolution of 40 µm) and pictures of its 3D-printed copy (B, D; spatial resolution of 29 µm).
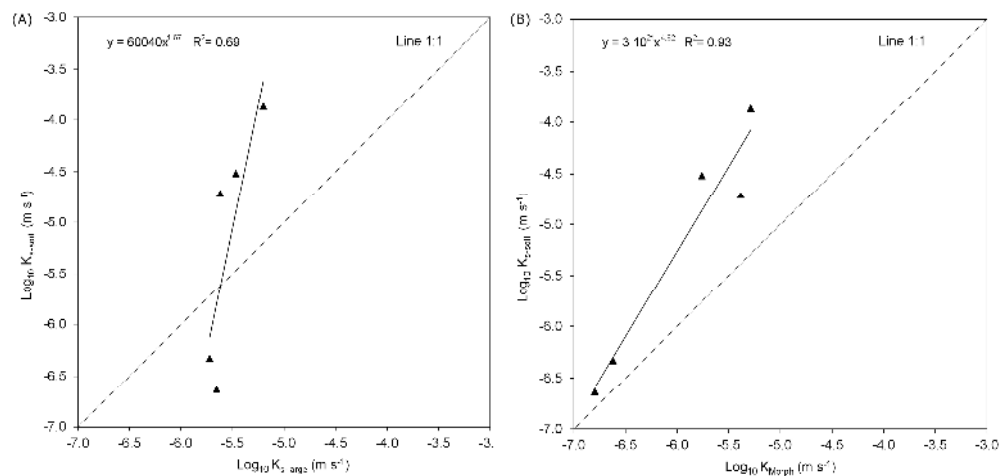118x130mm (300 x 300 DPI)

Figure 6 Relationship between saturated water conductivities estimated on soil-like prototypes (Ks-large, m s-1) and on the original soil samples by means of (A) experimental (Ks-soil, m s-1) and (B) modelling (KMorph, m s-1) approach.
317x152mm (300 x 300 DPI)